ACSNANO

www.acsnano.org

ARTICLE

Two-Dimensional Electron–Hole Plasma in Colloidal Quantum Shells Enables Integrated Lasing Continuously Tunable in the Red Spectrum

Ivo Tanghe,* Korneel Molkens, Tom Vandekerckhove, Dobromił Respekta, Amelia Waters, Jiamin Huang, Jacob Beavon, Dulanjan Harankahage, Chao Yang Lin, Kai Chen, Dries Van Thourhout, Mikhail Zamkov, and Pieter Geiregat

Cite This: *ACS Nano* 2024, 18, 14661–14671

Read Online

ACCESS | Metrics & More | Article Recommendations | Supporting Information

ABSTRACT: Combining integrated optical platforms with solution-processable materials offers a clear path toward miniaturized and robust light sources, including lasers. A limiting aspect for red-emitting materials remains the drop in efficiency at high excitation density due to non-radiative quenching pathways, such as Auger recombination. Next to this, lasers based on such materials remain ill characterized, leaving questions about their ultimate performance. Here, we show that colloidal quantum shells (QSs) offer a viable solution for a processable material platform to circumvent these issues. We first show that optical gain in QSs is mediated by a 2D plasma state of unbound electron–hole pairs, opposed to bound excitons, which gives rise to broad-band and sizable gain across the full red spectrum with record gain lifetimes and a low threshold. Moreover, at high excitation density, the emission efficiency of the plasma state does not quench, a feat we can attribute to an increased radiative recombination rate. Finally, QSs are integrated on a silicon nitride platform, enabling high spectral contrast, surface emitting, and TE-polarized lasers with ultranarrow beam divergence across the entire red spectrum from a small surface area. Our results indicate QS materials are an excellent materials platform to realize highly performant and compact on-chip light sources.

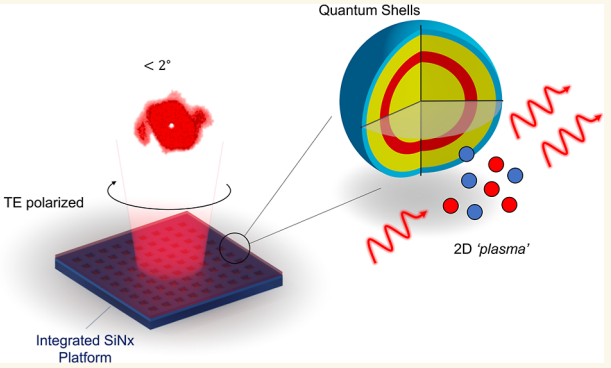

KEYWORDS: *quantum shell, nanocrystal, optical gain, lasing, integrated photonics, photonic crystal*

INTRODUCTION

With the advent of laser projection, augmented or virtual (AR/VR) reality headsets, and quantum communication, an increased demand for small footprint, bright, and highly collimated visible light sources is emerging. Moreover, such sources should be matched to very specific spectral bands, e.g. 620–640 nm to obtain pure red. Combining solution processable semiconductor gain materials with the diversity of scalable and miniaturization-driven integrated photonics platforms available today presents a promising route forward. In particular, the use of colloidal nanomaterials has pioneered this hybrid approach, showing optically pumped on-chip lasing, both with in and out-of-plane emission,[1−3] and even demonstrations of electrically driven amplification.[4] Such results are proof of a continued pursuit of more effective optical gain metrics and materials, resulting in the development of a diverse range of nanocrystals with varying elemental compositions[5] and structural configurations, e.g., by incorporating semiconductor shells to exploit charge separation,[6,7] or by changing the geometry from 0D to 2D, leading to different photophysical mechanisms for light amplification.[8,9] To understand what is lacking today, we can categorize these materials based on three nonlinear optical material parameters: the inverted-state (or gain −) lifetime, τ_G, the threshold carrier

Received: March 1, 2024
Revised: May 1, 2024
Accepted: May 10, 2024
Published: May 23, 2024

https://doi.org/10.1021/acsnano.4c02907
ACS Nano 2024, 18, 14661–14671

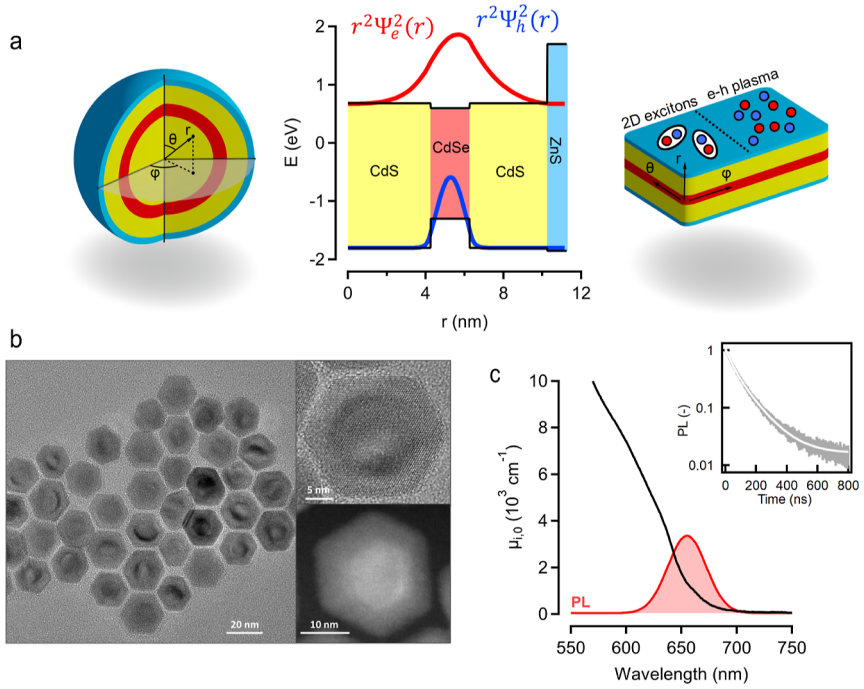

Figure 1. Structural and linear optical characterization of QS samples used in this work. (a) Schematic in spherical coordinates and wave function localization for electron (blue) and hole (red) of the various layers constituting the QS-S particle, with a final cartoon (right) showing the possible 2D carrier species that can coexist in the planar equivalent of the spherical QS system: Coulomb-bound 2D excitons or uncorrelated electrons and holes forming a 'plasma' state. (b) Transmission electron microscopy (TEM) imaging of the QS-S sample. (c) Linear absorption spectrum, expressed as the intrinsic absorption coefficient $\mu_{i,0}$ and the spontaneous emission or photoluminescence (PL) spectrum after 400 nm excitation. Inset shows the PL decay after 400 nm excitation, indicating an amplitude weighted average lifetime of 87 ns.

density, n_{th}, required for transparency, and the material gain coefficient, g_i. A recent report by Tanghe et al. provided a combination of record metrics on all fronts in a single material using bulk CdS nanocrystals.[3] In these materials, the optical gain originated from a plasma state, i.e. a collective of unbound electrons and holes, and not from well-defined Coulomb-bound excitons. Moreover, the gain lifetime was not limited by non-radiative processes, such as Auger recombination, but dictated by fast second-order radiative recombination. Given the limitations of the bulk concept, which gives up emission wavelength variation through size change, these demonstrations are, however, limited to the green spectral window for now. To extend toward full RGB coverage, the quest for a comparable candidate providing excellent gain metrics across the board in the red spectrum without a non-radiative quench at high densities is still actively ongoing.

The extensive family of CdSe-based materials can provide a solution. Indeed, as of today, quantum dots (QDs) of CdSe/CdS or CdSe/ZnSe,[10] where size confinement leads to discrete energy levels and well-defined exciton states, already bring a compromise solution in terms of the gain metrics. They offer gain lifetimes close to 1 ns, material gains of ca. 1.000 cm^{-1}, and thresholds close to 1 exciton per particle. These metrics are driven mainly by small biexciton redshifts of less than 10 meV.[6] Nonetheless, the gain lifetime is also limited by non-radiative Auger quenching. Quantum wells of CdSe, so-called nanoplatelets, can also be pushed to the red spectrum by increasing layer thickness,[11] but a more promising route seemed to be shelling a thinner core platelet with CdS layers on both sides, so-called platelet-in-box systems.[12] Using these materials, efficient red lasing action was demonstrated, although demonstrations of quasi-continuous wave (quasi-CW) operation or a deeper understanding of their photophysics remain absent today.[13] For example, it remains unclear whether the observed ca. 1 ns gain lifetimes are limited by a radiative process or not. Within this material class, spectral tuning through variations of the layer thicknesses, as well as passivation of edge states, is also not straightforward.[14]

CdSe-based quantum shells (QSs) combine the 2D delocalization, akin to the platelet-in-box systems, with a high, near-unity, quantum yield and the ability to maintain tuneability of the band gap in the technologically relevant red part of the spectrum.[15] Figure 1a shows a cartoon of the QS geometry, where a core of CdS (yellow) is capped with subsequent layers of CdSe (red), CdS (yellow), and finally a protective layer of ZnS (blue). Due to the band offsets between CdSe and CdS, charge carriers are effectively confined radially while keeping full delocalization in the rotational degrees of freedom (θ, φ), as shown in Figure 1a (middle). As validated through time-resolved fluorescence experiments, these materials showed slow, if not fully absent, recombination of multicarrier species and were hence primed for use in scintillation and lasing, though clear demonstrations of the latter are absent to date.[15] Previously published results already indicated an ability for amplified spontaneous emission, leaving the question of whether lasing can be achieved open. Next to this, long material gain lifetimes of up to 6 ns were found in the solution phase.[15] It is, however, not clear what QS can truly bring in terms of the remaining key gain metrics, i.e., the material gain coefficient g_i and gain threshold, a problem intimately linked to a lack of understanding of the photophysics underlying their light-matter interactions. If we

https://doi.org/10.1021/acsnano.4c02907
ACS Nano 2024, 18, 14661−14671

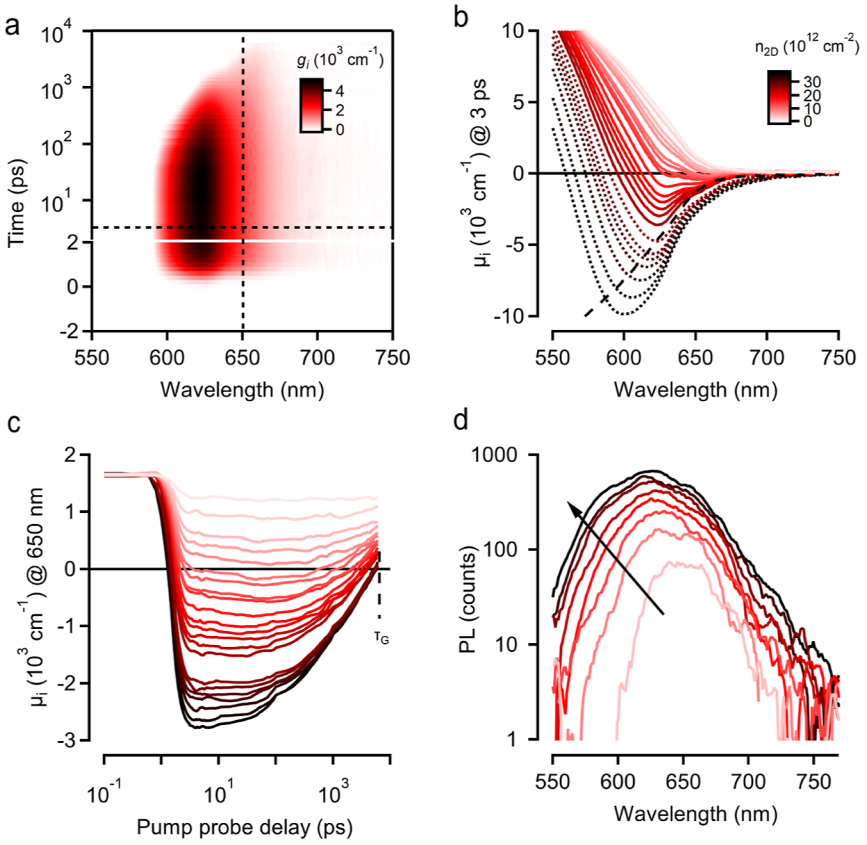

Figure 2. Ultrafast optical spectroscopy of QS samples in dilute dispersion. (a) Gain map of the QS-S sample after 515 nm photoexcitation, creating 29 electron−hole pairs per QS. False color represents the material gain coefficient g_i in cm^{-1}. Dashed lines indicate the temporal and spectral positions used in (b,c), respectively, to represent the gain spectra and dynamics for increasing carrier density. (b) Intrinsic absorption at 3 ps time delay, showing net gain ($\mu_i < 0$) manifests from around 3 electron−hole pairs per QS on average or a surface density n_{2D} of 1.3 × 10^{12} cm^{-2} and stretches from 560 to 700 nm for the highest densities used. The dashed black line represents $\mu_{i,0}$ and is a natural guide to the eye for the maximum achievable gain in a system without spectral shifts. Dashed lines indicate gain spectra exceeding the $\mu_{i,0}$ limit, indicating stronger shifts do occur at extreme fluence. (c) Dynamics of the intrinsic absorption after increasing photoexcitation density, showing that at the highest flux net optical gain can be sustained up to and beyond 6 ns, labeled here as the gain lifetime τ_G, which is also the maximum of the experimental delay stage used. (d) PL captured 3 ps after photoexcitation for increasing carrier density showing a broad and fluence dependent (arrow direction) window stretching from 550 nm, limited by a long-pass cutoff filter, to ca. 750 nm.

consider them as 2D semiconductors, are the photophysics dominated by excitons, as in core platelets,[8] or do we have to consider unbound electron−hole pairs, a mechanism prompted for more similar 2D platelet-in-box systems and bulk CdS nanocrystals?[3,9]

Here, we first rationalize QSs[15,16] as high-quality red spectrum gain materials by quantitative femtosecond spectroscopy on QS architectures with varying CdS core size. Our results show first of all that optical gain is indeed limited by a very slow relaxation process on the multiple-nanosecond time scale, outpacing competing planar platelet-in-box systems. Through a delicate global fitting of pump−probe data and a fluence-dependent PL analysis, we can assign this cap to the gain lifetime of a 2D electron−hole radiative recombination process. Such a mechanism strongly contradicts earlier claims that non-radiative Auger processes would be important. Next, the gain threshold is rationalized within the same concept of 2D unbound electron−hole pairs being the dominant species, showing that the QS indeed behave as nonexcitonic 2D semiconductors. Building on these fundamental insights and a rational choice of optimal QS geometry, broadband lasing over a wide spectral region in the red (580−660 nm) is demonstrated on a fully integrated silicon nitride (SiNx) platform using optical pumping with green light (515 nm) of photonic crystal surface emitting laser cavities (PCSEL) coated with QS material. Thresholds as low as 15.9 μJ/cm^2 for femtosecond excitation and 67 kW/cm^2 for quasi-CW (7 ns) operation are obtained. Finally, the out-of-plane laser emission is characterized as highly polarized with an ultranarrow beam divergence of less than 2° in the far field. A detailed finite-difference-time-domain (FDTD) study backs these observations quantitatively, summarizing our full understanding of both the materials and device aspects of hybrid QS-PCSEL lasers.

RESULTS AND DISCUSSION

In this work, we focus on two distinct variations of the QS geometry by varying the CdS inner core diameter d_{CdS} from 8.5 to 20 nm, see Figure 1a, which we label as small (QS-S) and large (QS-L), respectively. The samples are synthesized according to the procedure laid out by Harankahage et al. and Cassidy et al.,[15,16] see also Methods and Supporting Information S1. The CdSe thickness slightly varies between 1.8 and 2 nm, as do the outer CdS/ZnS surface barrier layers. This leads to a slightly larger band gap for the QS-L sample. Figure 1a shows how electrons and holes are localized throughout the

https://doi.org/10.1021/acsnano.4c02907
ACS Nano 2024, 18, 14661−14671

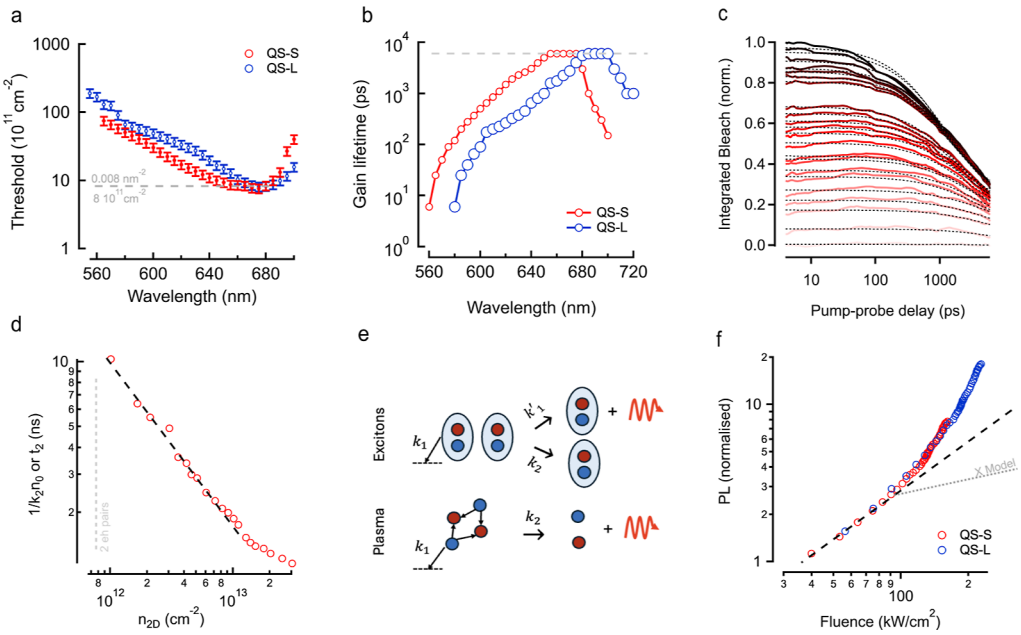

Figure 3. Modeling optical gain in QS systems. (a) Threshold density in electron−hole pairs per cm^2 to achieve optical gain in the QS-S and QS-L sample as a function of wavelength. Horizontal dashed line indicates the lowest density required for net gain, the 'threshold'. (b) Gain lifetime, see also Figure 2c, extracted at varying wavelengths for both the small (QS-S, blue) and large core (QS-L) sample, showing a comparable trend apart from a small redshift due to the thicker CdSe region in QS-L. (c) Integrated TA bleach dynamics of the QS-S sample after 515 nm photoexcitation with a global fit model imposed assuming only second order recombination. (d) Extracted initial two-body recombination time $\tau_2 = 1/(k_2n_0)$ plotted versus the initial 2D sheet density. (e) Cartoon depicting the nature of the second order recombination k_2 in an exciton picture (top) and free carrier "plasma" picture (bottom). (f) Normalized PL counts of strongly diluted dispersions of QS-S and QS-L, excited with quasi-CW 7 ns pulses at 532 nm. Dashed black line indicates a linear trend, whereas the dotted gray line shows a square-root dependence.

QS-S particle as a function of the radial coordinate r, indicating strong localization of holes in the CdSe surface area, whereas electrons tend to delocalize somewhat more over the CdS barriers. In what follows, we will normalize carrier populations to the CdS core surface area (πd_{CdS}^2) to represent the 2D area over which charge carriers effectively delocalize in QS systems. We note that this surface area is increased by a factor of 5.5 on going from the QS-S to the QS-L sample. Figure 1b shows a TEM image of the QS-S sample, indicating its high structural quality. Next, Figure 1c shows the absorption spectrum of the QS-S sample, normalized to represent the intrinsic absorption coefficient $\mu_{i,0}$, see Supporting Information S2. The sample emits at 655 nm, see Figure 1c with a quantum yield of over 80%. Using time-resolved luminescence in a regime of single excitons per QS, we find an average lifetime of 87 ns; see inset Figure 1c.

We first study the development of net optical gain by means of quantitative transient absorption spectroscopy (TA), in line with previous reports.[3,5,6] In short, a 170 fs pulse at 515 nm (2.4 eV) is used to excite a QS dispersion, creating a population of electron−hole pairs. After the initial pump pulse, a second time-delayed probe pulse is used to measure the difference in absorbance $\Delta A(\lambda, t)$ as a function of wavelength (energy) and time. By adding to ΔA the linear absorbance A_0, we obtain the actual sample absorbance $A(\lambda, t)$, which can be normalized using the intrinsic absorption coefficient to represent the material gain $g_i(\lambda, t) = -\mu_i(\lambda, t)$, as shown via a false color map in Figure 2a for a high excitation density of 29 electron−hole pairs per QS. A broad spectral region opens up where net gain is observed, stretching up to multiple nanoseconds in time on the red edge. In Figure 2b, spectral slices of the intrinsic absorbance are shown for a 3 ps pump−probe delay for multiple excitation densities, expressed here as the average number of electron−hole pairs $\langle N \rangle$ per QS CdS surface area particle created at time zero. At high density, a broad gain window stretches from 550 to 680 nm, showing no signs of saturation of the gain coefficient. The dashed black line in Figure 2b represents $\mu_{i,0}$ and is a natural guide to the eye for the maximum achievable gain in a system without spectral shifts. The dashed color lines indicate gain spectra exceeding the $\mu_{i,0}$ limit, indicating strong spectral shifts do occur at extreme carrier densities above ca. 10^{13} cm^{-2}, a feat we assign to strong band gap renormalization as observed in both bulk and 2D semiconductors alike.[3,17] In Figure 2c, an example kinetic trace is shown at 650 nm near the band gap. Where the trace crosses transparency ($g_i = 0$), we define the gain lifetime τ_G, which, for the best case (670 nm), is limited by the maximum time delay in our experiment (6 ns). Figure 2d shows a similar experiment to the TA, where now the PL emitted by the dispersion is collected 3 ps after photoexcitation with 515 nm; see Methods. We observe that the PL of a strongly excited QS sample stretches out over the same spectral windows as the optical gain shown in Figure 2b. Similar results are obtained on the QS-L sample, as shown in Supporting Information S3.

Given their overall spherical shape, optical gain in CdSe-based QS is often described in terms of those models used to describe state-filling gain in zero-dimensional CdSe QDs with discrete energy levels, using terminology such as biexcitons, S/P/D/...-states, and multiexciton Auger recombination.[15,16] It is, however, very unlikely that these mechanisms are correct to describe the massively delocalized electron−hole pairs that

https://doi.org/10.1021/acsnano.4c02907
ACS Nano 2024, 18, 14661−14671

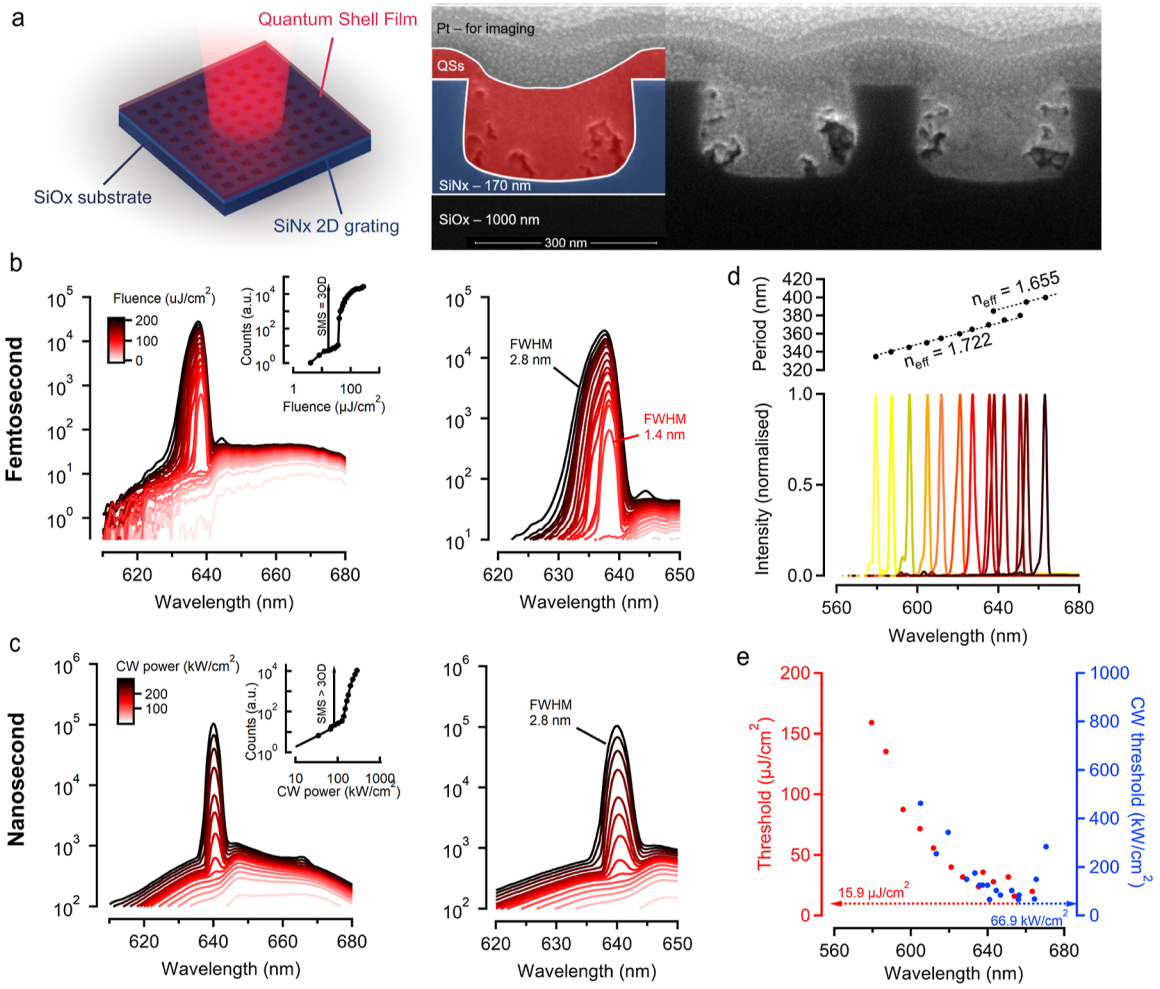

Figure 4. Quantification of lasing action in QS-PCSELs under pulsed excitation. (a) Sample sketch (left) and a cross-section taken with SEM, showing the QS layer in red and the SiNx photonic crystal surface layer in blue. (b) Spectra under various femtosecond excitation strengths for the device with a period of 385 nm, over the full spectrum (left) and a zoom around the lasing peak (right). The inset shows the peak counts increasing pump flux. (c) Similar to (b) but with quasi-CW excitation using 7 ns pulses at 532 nm. (d) Normalized lasing peaks with their corresponding photonic crystal lattice period. A distinct jump is observed in the effective index going from 380 to 385 nm. (d) Femtosecond (red) and quasi-CW (blue) thresholds for all devices, showing clear correlation and minima in the 640−660 nm window.

occupy highly degenerate electronic states due to the lack of in-plane confinement. The latter is better seen as the absence of confinement in the rotational degrees of freedom (θ, ϕ), as sketched in Figure 1a. Given this type of carrier confinement of electrons and holes in QS samples, we argue that optical gain is mediated by either 2D excitons, center-of-mass delocalized Coulomb-bound electron−hole pairs, or a gas of unbound electron−hole pairs, often denoted as a "plasma" state—confined to 2D, see Figure 1a (right). For example, due to the high exciton binding energy of ca. 200 meV, optical gain in core-only 2D CdSe nanoplatelets is mediated by an exciton-driven mechanism,[8] where at high density, excitons fuse together into molecule states to provide red-shifted gain and a retention of the exciton absorption lines associated with the heavy and light-hole transitions.[18] On the other hand, gain driven by a plasma mechanism is quite classical and follows textbook semiconductor descriptions where gain originates from state-filling of electron and hole states. Geuchies et al. showed that gain in platelet-in-box systems (CdS/CdSe/CdS) follows this latter mechanism, mainly due to the weakened Coulomb interaction as a consequence of carrier separation and increased dielectric screening, resulting in exciton binding energies in the order of only 40 meV.[9]

A first identification of the nature of the gain mechanism can be found in rationalizing the threshold required for the net optical gain. First off, optical gain requires a large number of electron−hole pairs $\langle N \rangle$ per QS (3.1 and 12 for QS-S, L respectively). This indicates that a simple 0D state filling model cannot be applied, as in such scenarios, a fixed number of carriers per QS would be required. Furthermore, for both the QS-S and QS-L sample, we find a common threshold flux of 7 μJ/cm^2, despite the massive difference in surface area and/or volume. If we normalize $\langle N \rangle$ to the CdSe QW area ($=\pi d_{CdS}^2$), see Supporting Information S2, we find a surface density n_{2D} of 0.008 electron/hole pairs per square nanometer (8×10^{11} cm^{-2}) is required to achieve gain at the band gap, both for the QS-S and QS-L samples, despite their factor 5.5 difference in the surface area. Apart from a spectral shift due to the smaller band gap of the QS-L sample, the threshold densities keep their match across the spectrum for both samples. Comparing these numbers to the established 2D plasma model of Geuchies et al., where the gain threshold is given by $n_{2D} = 0.013$ nm^{-2} (or 1.3×10^{12} cm^{-2}, see Supporting

https://doi.org/10.1021/acsnano.4c02907
ACS Nano 2024, 18, 14661−14671

Information S4 and Figure S3) irrespective of area,[9] we can rationalize that the found universal surface density dependent gain threshold indicates gain is linked to unbound 2D electrons and holes, or a 2D plasma like state. Note that this does not necessarily imply that excitons cannot coexist at lower absolute occupation numbers per QS particle since the Mott transition point for 2D excitons in CdSe is around 0.02 excitons/nm^2, see Supporting Information S5.

Finally, the continuous density of states (DOSs), implied by the 2D "plasma" model, is also prevalent in the gapless solution and thin film gain spectra, as shown in Supporting Information S8. This contrasts the often band-like amplification spectra found for strongly confined systems.

Figure 3b shows the gain lifetime extracted for both samples, showing a continuously varying wavelength dependence and a cap at the experimental limit of 6 ns; see Methods. If we continue our assumption that optical gain at higher carrier densities in QS is indeed mediated by an unbound electron−hole plasma, we can also more carefully rationalize the limiting processes to optical gain. In general, the recombination dynamics of a surface carrier density n are described by

$$-\frac{dn}{dt} = k_1 n + k_2 n^2 + k_3 n^3 \quad (1)$$

Figure 3c shows the dynamics of the integrated bleach for increasing carrier density measured on the QS-S sample, subject to a global fit where $k_3 = k_1 = 0$, see Supporting Information S6. The fit produces a value for k_2, the second order process, which can be directly linked to an initial 2-body recombination time $\tau_2 = 1/(k_2 n_0)$, as plotted in Figure 3c, where n_0 is the excitation surface density (in cm^2) at time zero. A value of 10^{-4} cm^2 s^{-1} is obtained, which is about 1 order of magnitude smaller than for nanoplatelets[18,19] and more in line with recent reports on indirect excitons in 2D transition metal dichalcogenides.[20] In the broad density regime where linearity is obtained, we can indeed model the recombination perfectly using only a second order process. At low surface density, the two-body recombination is quite inefficient leaving a > 10 ns lifetime, speeding up to below 2 ns at higher density. We note that a surface density of ca. 5×10^{11} cm^{-2} in fact corresponds to having a "bi-exciton" type state in the QS, i.e., two electrons and two holes. We should be careful with this nomenclature. As sketched in Figure 3e, for a plasma state k_1 refers to the trapping rate, k_2 refers to radiative electron hole ($np = n^2$) recombination and k_3 is linked to 3-particle Auger processes (e.g. $nnp = ppn = n^3$). In excitonic 2D materials, such as transition metal dichalcogenides[20] or core-only nanoplatelets,[8,18] the interpretation of these terms $k_{1,2}$ is however quite different, see Supporting Information S6, as k_1 refers to both trapping and radiative recombination (labeled in Figure 3e as k_1') and k_2 is seen as non-radiative exciton−exciton annihilation, i.e., Auger recombination. As such, a priori, our observation of a second order process could be both a detrimental Auger sink or a very useful radiative process. To distinguish between both, we carried out quasi-CW PL experiments, see Supporting Information S7, on dilute dispersion of both QS samples. Figure 3f shows the result of the integrated PL as a function of fluence, expressed as kW/cm^2. Initially, a linear trend is observed. However, at high density a clear disruption is seen toward a quadratic increase of the PL intensity. Such behavior contrasts strongly with the expected decrease of PL intensity in an Auger scenario for k_2, as indicated by the gray dashed line, see Supporting Information S7. As such, we conclude that the limit on the lifetime of multicarrier states, and hence optical gain, in QS systems is not classical Auger recombination but instead a highly desirable accelerated radiative recombination of unbound electrons and holes.

Using the QS-S sample, we continue to fabricate photonic crystal surface emitting lasers, or PCSELs in short, using a silicon nitride (SiNx-on-SiOx) photonic platform.[1−3] A square lattice 2D photonic crystal (PhC)-type cavity is used,[21,22] similar to previous demonstrations in literature.[3,23,24] Here, holes are etched periodically into a low loss 170 nm thick SiNx film on SiOx; see Figure 4a, featuring periods spanning from 320 to 460 nm with 5 nm intervals. These gratings are then overcoated with a QS layer through spin-coating forming QS-PCSEL devices. Through cross-sectional SEM imaging, see Figure 4a, a duty cycle of around 70% is found, and clear infilling is confirmed. The resonating wavelength within such cavities follows Bragg's Law: $m \cdot \lambda_{Bragg} = 2 n_{eff} \Lambda$. Here, m denotes the order of diffraction, λ_{Bragg} is the resonant wavelength, n_{eff} is the effective refractive index of the structure, and Λ is the period of the grating. A second order grating was used to achieve surface emission. Laterally, the devices are 600 × 600 periods, varying from 192 × 192 to 276 × 276 μm^2. First, the QS-PCSELs were pumped using the same 170 fs pulsed excitation at 515 nm as that used in TA. A typical result is shown in Figure 4b showing lasing at 637.5 nm with strong threshold behavior at 35.8 μJ/cm^2, see inset. Figure 4b further provides a closer zoom of the lasing peak, revealing an additional side peak emerging at higher fluencies broadening the lasing peak up from 1.4 to 2.8 nm fwhm. Varying the crystal period, lasing was obtained from 580 to 660 nm, in line with the gain window, see Figure 2b. Figure 4d displays the normalized lasing peaks for all devices, where the top graph connects period and resonance wavelength according to the Bragg law. Transitioning from a 380 nm to a 385 nm period results in a shift back to shorter wavelengths. Figure 4e shows the lasing thresholds for femtosecond excitation in red, revealing the lowest threshold within the range of 640−660 nm, measured at 15.9 μJ/cm^2. Subsequently, the same devices were pumped with a 100 Hz, 7 ns pulsed laser at 532 nm. Given that the pulse duration matches the longest gain lifetime found (ca. 6 ns), this excitation scenario involves the creation and annihilation of electron−hole pairs multiple times within a single excitation pulse. From an optical perspective, the process results in the formation of a stable optical mode, termed quasi-CW excitation. The results of this regime are listed in Figure 4c. Here, power density is given as the CW equivalent power or energy/pulse duration in kW/cm^2. Once again, lasing is observed with a threshold of 125 kW/cm^2. Figure 4e further summarizes the quasi-CW threshold, represented by blue dots. Quasi-CW lasing was obtained from 600 to 670 nm with a lowest observed threshold at 660 nm of only 66.9 kW/cm^2, a value corresponding to the tipping point of the solution-based PL in Figure 3f, indicating, as expected, a regime of multiple electron−hole pairs per QS. Finally, we note that the lasing emission does not saturate for quasi-CW excitation even after a 3 order of magnitude surge in emission intensity, e.g., in Figure 4c. This feat can be attributed to the accelerated radiative recombination of the plasma state, giving more photons back at a high pump rate instead of heating the device through Auger processes. A stability check was performed; see Supporting Information S9, where, after a million shots of

https://doi.org/10.1021/acsnano.4c02907
ACS Nano 2024, 18, 14661−14671

the 7 ns quasi-CW excitation source, no drop in performance was seen.

Apart from low thresholds and high spectral contrast, lasers in the RGB spectrum also require narrow beam divergence and well-defined polarization, e.g., to be used in laser projection or AR/VR applications. Figure 5a,b shows far field patterns

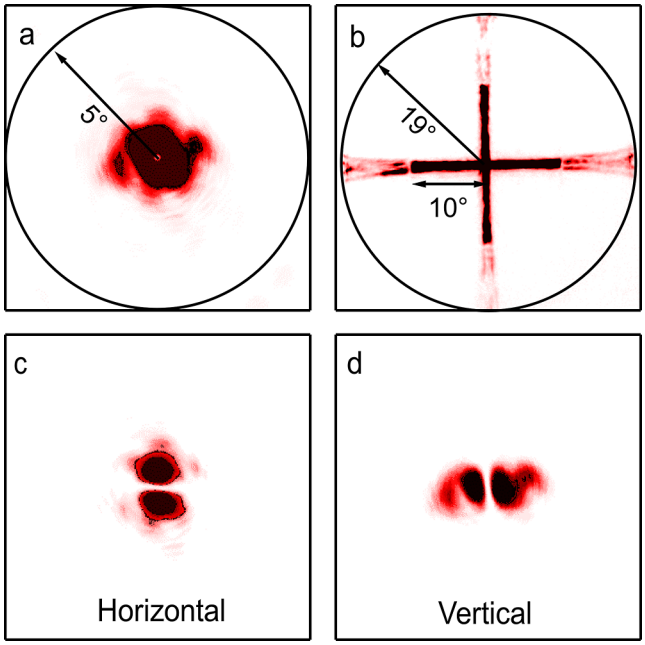

Figure 5. Out-of-plane emission of PCSEL device with a period of 395 nm collected using a room temperature CMOS 1.3 Megapixel array camera at 30 cm distance. (a) Collection above threshold without a polarizer showing highly collimated emission with beam divergence below 2°, defined relative to the normal on the PCSEL surface, showing a typical far field found for the devices with periods 385−405 nm. (b) Far field pattern measured with shorter periods (350−380 nm) above threshold. (c,d) Polarized version of the emission pattern in (a), now taken using either horizontal (c) or vertical (d) polarizer settings.

collected without using a polarizer in the collection path to investigate these points in detail. Above lasing threshold, a clear ring shape pattern is obtained for the devices with a larger period (385−405 nm) with an extremely small divergence angle, below 2°, a typical observation for PCSELs, which merits their use over, e.g., more commonly used VCSEL architectures.[13] For the shorter period devices (350−380 nm) lasing at shorter wavelengths, a cross-shape pattern appears above threshold, as shown in Figure 5b. Using a linear polarizer in the emission path (Figure 5c,d), we observe a distinct polarized response of the far field pattern.

In order to better understand these promising far field results, we simulated the photonic band structure with FDTD methods; see Supporting Information S10.1. By exciting all optical modes for a specific in-plane wave vector $\vec{k}_{||}$, we can identify resonances at distinct frequencies and reveal the photonic bands. Our approach involved traversing from the *M*-point $\left(\frac{\pi}{a}, \frac{\pi}{a}\right)$ to the Γ-point (0,0), and subsequently to the *X*-point $\left(\frac{\pi}{a}, 0\right)$,[25,26] which are the boundaries of the first Brillouin zone of the square photonic crystal. Figure 6a illustrates these findings, specifically for a period of 395 nm, zoomed in around Γ, which corresponds to upward scattering. Our analysis shows eight bands, corresponding to four transverse electric (TE) bands, while the remaining four represent transverse magnetic (TM) bands. These feature in-plane electric fields or magnetic fields for the TE bands or TM bands, respectively. Two pairs of modes (E_1 and E_2) become degenerate at Γ, resulting in six possible resonance points.[25,26] The designations (*A*, *B*, and *E*) specifically correspond to the symmetry of the in-plane fields. *A* and *B* modes exhibit antisymmetrical electric fields for TE (magnetic fields for TM) concerning the in-plane axis, whereas *E* modes feature symmetrical electric fields for TE (magnetic fields for TM). The antisymmetry induces destructive interference for upward scattering light, essentially rendering it forbidden. Consequently, for *A*/*B*-modes, light is effectively confined within the Photonic Crystal, resulting in an infinite *Q*-factor for an infinite number of periods. When ignoring scattering, in a finite device, the *Q*-factor will still not be infinite since this perfect antisymmetry is broken near the edge. For the *E*-modes, the situation differs, as there is a nonzero out coupling that serves as a loss mechanism, leading to significantly lower *Q*-factors even for an infinite structure. Increasing the period causes the entire band structure to shift downward in frequency or to longer wavelengths. In relative terms, this shift corresponds to the gain band moving upward in the band diagram, as illustrated in Figure 6a by the gray band. By selectively exciting the six modes at the Γ-point separately for various periods, an attempt can be made to align them with the experimentally measured lasing peaks, as explained in more detail in Supporting Information S10.1. The impact of the PhC on the spontaneous PL trace collected out-of-plane can be examined to verify this, as illustrated in Figure 6b,c, since lasing is a highly nonlinear and dynamic competition between all these modes. It can be observed in Figure 6c that with an increase in the period, the PL trace undergoes alterations compared to the PL from the bare substrate (slab, bottom black trace). This suggests a nuanced interplay between the PL from the QS layer and the emission direction permitted by the cavity. Especially for periods of 385 nm and beyond, distinctive additional features become evident on the traces: a two-peak pattern with a noticeable dip, which is attributed to the overlap between the positions of the TE *A* and *B* bands at the Γ-point and the PL spectrum, as out-coupling the PL at this point is forbidden. As such, there will be less PL at this particular wavelength, until threshold is reached. The PL curves shown in Figure 6c are normalized, but their maximum is displayed on the right. Longer period devices reach nearly 5 times the count rate of shorter periods due to the PL of the QSs overlapping with numerous photonic bands, resulting in a high DOSs near the Γ-point. The combination of the antisymmetrical electrical field for the *A*/*B* modes, which leads to the local dip in the PL, along with the enhancement of the PL around this dip due to a high DOS, aligns well with the experimental data. Notably, the distinct dip in the PL aligns precisely with the position of the lasing; see also Figure 6b, reinforcing the notion that this corresponds to the TE *A* or *B* mode.

Turning the focus now to the lasing peaks, simulations for the six resonant modes across different periods are illustrated as circles (*A*), diamonds (*B*), and crosses (*E*) in red (TE) and blue (TM), superimposed with the measured lasing peaks represented by black asterisks in Figure 6d. Excellent alignment is observed between the simulation and the experiment. Devices in the range of 350−380 nm coincide with the TE *E*

https://doi.org/10.1021/acsnano.4c02907
ACS Nano 2024, 18, 14661−14671

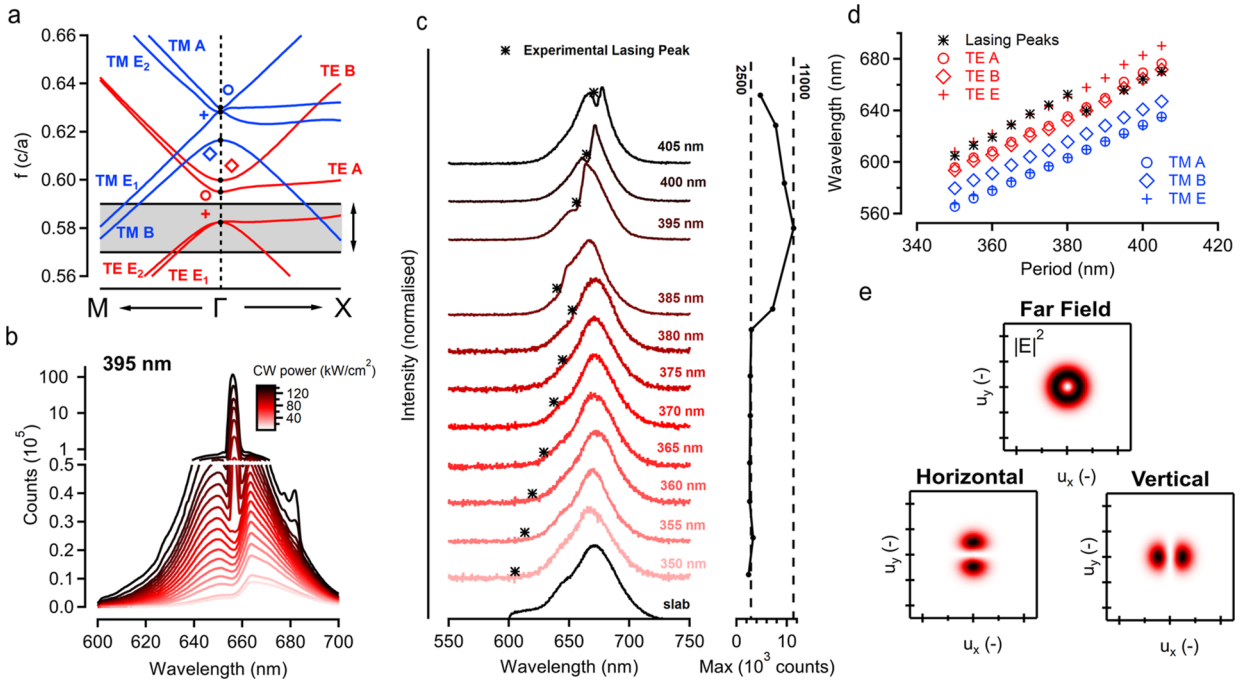

Figure 6. Modeling of lasing in QS-PCSELs (a) Photonic band structure going from *M* to Γ to *X*. (b) Spectra under various excitation strengths at 395 nm, particularly focused on the PL showing a clearly visibledip at 659 nm below lasing threshold. (c) PL spectra for various photonic crystal lattice periods (color curves) with the indication of measured lasing wavelength (black asterisks). The curve on the right shows the maximum counts measured for each period. (d) Simulated (red and blue markers) and experimental lasing peak (black diamonds) as a function of period, showing excellent agreement. (e) Far field patterns for TE A/B modes at the Γ-point for our device, including their horizontal and vertical polarized counterparts.

mode, while those in the 385−405 nm range align with the TE *A* or *B* mode. Despite the theoretical possibility of TM lasing in this scenario, no such observation was made, as further confirmed by the polarization-resolved experiments. Indeed, specifically for the *A*/*B* modes, it is well known that the far field of a device with symmetrical shapes in a unit cell will manifest a ring shape.[3,27] Conversely, for the *E* mode, it assumes the form of a Gaussian. The cross shape of Figure 5b has previously been explained by Riechel et al.,[28] and is discussed in more detail in Supporting Information S10.2. Although the characteristic ring shape is the same for both the TE and TM modes, their polarization differs. The TE far fields have azimuthal polarization, while for TM, it is radial. Subsequently, with the introduction of a linear polarizer, it becomes possible to discern whether the observed ring in the far field is the result of TE or TM modes. Figure 6e (top) illustrates a simulated far field, showing the typical ring shape, and Figure 6e (bottom) shows the simulated far field when it is horizontally polarized (left) or vertically polarized (right). This can be directly compared with the measurements shown in Figure 5. When we apply horizontal polarization, distinct vertical lobes emerge, and vice versa. This observation serves to confirm the TE nature of the mode. The absence of the TM mode lasing toward larger periods is ascribed to the higher intensity of the electric fields near the surface for these modes. This phenomenon, combined with the surface roughness, which can be seen in Figure 4a, leads to more scattering relative to TE modes, thereby tilting the mode competition in favor of TE.

CONCLUSIONS

In this study, we investigated the optical gain mechanisms in colloidal QSs and used them to demonstrate highly efficient integrated laser devices. Our findings not only confirm the long gain lifetimes previously observed for QS materials[15] but also unveil that this lifetime is capped by a radiative process, not detrimental Auger relaxation. Next, we identify the nature of the gain mechanism as stimulated emission originating from 2D unbound electron−hole pairs, not excitons, where, in particular, their surface density is crucial. Moreover, we uncover a high material gain, stretching to 10.000 cm^{-1}, over a broad bandwidth, thereby surpassing benchmarks set by competing red-emitting colloidal QDs[4,6,29] and platelet-in-box systems.[13] We argue QS systems are quite similar to platelet-in-box architectures, but a proper quantification of the latter is still required to make this claim more confidently. The QS was used as a gain material on an integrated silicon nitride-based platform with an optical cavity based on a compact, surface-emitting PCSEL design. Lasing is achieved in ambient conditions with both femtosecond and quasi-CW operation, showcasing competitive thresholds across the full red spectrum in comparison to the best reported devices in the literature[2,3,23] Importantly, due to the lack of non-radiative quenching at a higher pump rate, the lasers show a clear lack of saturation in their emission and very high stability. They also retain a highly collimated and polarized output beam, enabling them for applications in far-field projection systems. Overall, colloidal QSs present an interesting platform to explore how weakly confined colloidal 2D semiconductors can enhance integrated photonic platforms to enable full-spectrum lasing. The extreme tunability of the QS geometry and the ease of changing the geometrical parameters, e.g., compared to more common

https://doi.org/10.1021/acsnano.4c02907
ACS Nano 2024, 18, 14661−14671

nanoplatelet syntheses, clearly present an exciting prospect for realizing high-quality optically pumped lasing across the entire visible spectrum.

METHODS

Materials Synthesis. Detailed information on the synthesis and structural characterization of the QS samples can be found in Supporting Information S1.

TA. Samples were excited using 170 fs pump pulses at 515 nm through second harmonic generation in alpha-BBO. Probe pulses were generated in a 2 cm thick YAG crystal using the 1030 nm fundamental. The pulses were delayed relative to the pump using a delay stage with a maximum delay of 6 ns for 515 nm pumping. The probe spectrum in our experiments covers the spectral window from 515 to 900 nm. The QSs were dispersed in an optically transparent solvent (hexane) and continuously stirred to avoid charging or photodegradation. The pump wavelength and sample concentration were chosen to obtain an optimal trade-off between having a good signal at the band−edge transitions, while still not having a too strong absorption at the pump wavelength to ensure uniform pumping of the sample. The average number of absorbed photons (or equivalently created excitons) at time zero, noted as $\langle N \rangle$, can be calculated from the photon flux J_{ph}, the cuvette length L and the nanocrystal absorption cross section at the pump wavelength σ_{λ_p}: $\langle N \rangle = J_{ph} \times \sigma_{\lambda_p} \times \frac{1 - e^{-\alpha_{0,\lambda_p} L}}{\alpha_{0,\lambda_p} L}$. The photon flux is calculated from the beam area, obtained through a Thorlabs CCD beam profiler, and corrected for reflections at the cuvette−air interface. The beam area is defined as $A_{beam} = 2\pi \times \sigma_x \sigma_y$, where σ_i is the standard deviation in the $i = x, y$ direction. Note that the carrier density n follows $\langle N \rangle / S$, with S being the surface area of the nanocrystal.

Time-Resolved PL Spectroscopy. For the TRPL, the samples were excited using a MaiTai femtosecond laser with a wavelength of 800 nm, which is frequency doubled to 400 nm. The laser has a repetition rate of 8 MHz and a pulse length of 110 fs. The signal is the center of the emission, and the spectrometer was fiber coupled to a time-correlated single photon detector (IDQ100). For the detection of the broadband PL transients on a subpicosecond time scale, we used the transient grating PL technique.[30] The output of a femtosecond ytterbium-based fiber laser (Amplitude, Tangerine SP) was split into pump and gate parts. For the pump part, second harmonic (515 nm) generation was used in the experiments and focused on a 225 μm^2 spot onto the sample. The PL signal from the sample was collected and refocused onto the gate medium, a 1 mm YAG crystal, by using a pair of off-axis parabolic mirrors. For the gate part, about 60 μJ of the 1030 nm output was split using a 50/50 beam splitter to generate the two gate beams and focused onto the gate medium at a crossing angle of approximately 8° and overlapped with the PL in a boxcar geometry. The two gate beams, which spatially and temporally overlap inside the gate medium, generate a laser-induced grating. This transient grating acts like an ultrafast optical shutter to temporally resolve the broadband PL signals by diffracting the gated signal from the PL background. The gated signals were focused onto the spectrometer entrance (Princeton Instruments SP 2150), and the transient PL spectra were measured with an intensified CCD camera (Princeton Instruments, PIMAX3). The time delay between the pump and gate beams was controlled via a motorized optical delay line. For each transient PL spectrum, 60 000 shots at each gate time delay were accumulated.

Photonic Crystal Cavity Fabrication. Silicon substrates with 1 μm silicon oxide are used as the starting chip. These are first cleaned using acetone and isopropanol, followed by an oxygen plasma treatment. By plasma-enhanced chemical vapor deposition, 180 nm of silicon nitride is deposited at 270 °C. To create the grating, electron beam lithography is used. First, the positive resist AR-P 6200.13 is used, spin-coated at 4000 rpm, to achieve resist thicknesses of 400 nm. The chip is then baked at 150 °C for 60 s. After this, AR-PC 5090 is spun as a protective coating, also at 4000 rpm, to achieve a layer around 40 nm thick. This conductive coating increases the electron beam lithography resolution. After spin-coating, the chip is baked at 90 °C for 120 s. E-beam lithography is done using a Raith Voyager system, using a dose of 160 $\mu C/cm^2$. After exposure, the chip is developed by putting it into a bath of n-amyl-acetate for 60 s, following an isopropanol bath for 60 s. A specifically optimized reactive ion etching process based on CF_4/H_2 chemistry is used to etch the silicon nitride layer and is almost etched completely through. After the etch, the remaining resist is cleaned off using an oxygen plasma treatment. Finally, the QSs are spin-coated on top of the chip, with a film thickness of about 50 nm.

Laser Measurements. For femtosecond excitation, the same 515 nm laser as above is used with 110 fs pulses. The beam is reflected on a dichroic mirror with a cutoff wavelength of 600 nm and is then focused perpendicular to the sample. The surface emission is transmitted through the dichroic. Following this, a 50/50 splitter is used, where 50% of the light is focused on a fiber for spectral analysis, and 50% is focused on a camera for imaging. The fiber went to an Andor Shamrock 750 spectrograph. The nanosecond excitation uses the same optical setup, but an Ekspla NL202 laser is used, with a fundamental at 1064 nm, and second harmonic generation through alpha-BBO doubles this to 532 nm. The pulse duration is 7 ns. Here, the signal is measured using an Andor Kymera 328i.

Photonic Crystal Simulations. Details on photonic band structure calculations are given in Supporting Information S10.

ASSOCIATED CONTENT

Data Availability Statement

The data that support the findings of this study are available from the corresponding author upon reasonable request.

Supporting Information

The Supporting Information is available free of charge at https://pubs.acs.org/doi/10.1021/acsnano.4c02907.

Overview of the sample's linear optical and structural characterization, more in-depth discussions on the recombination models, Mott density concepts and gain threshold modeling, amplified spontaneous emission experiments, stability measurements of the lasers, and detailed explanation on the photonic crystal simulations (PDF)

AUTHOR INFORMATION

Corresponding Author

Ivo Tanghe − *Photonics Research Group, Ghent University, Gent 9000, Belgium; Physics and Chemistry of Nanostructures and NOLIMITS Core Facility for Non-Linear Microscopy and Spectroscopy, Ghent University, Gent 9000, Belgium;* orcid.org/0000-0001-9241-5585; Email: ivo.tanghe@ugent.be

Authors

Korneel Molkens − *Photonics Research Group, Ghent University, Gent 9000, Belgium; Physics and Chemistry of Nanostructures and NOLIMITS Core Facility for Non-Linear Microscopy and Spectroscopy, Ghent University, Gent 9000, Belgium*

Tom Vandekerckhove − *Photonics Research Group, Ghent University, Gent 9000, Belgium*

Dobromił Respekta − *Physics and Chemistry of Nanostructures and NOLIMITS Core Facility for Non-Linear Microscopy and Spectroscopy, Ghent University, Gent 9000, Belgium*

Amelia Waters − *Department of Physics, Bowling Green State University, Bowling Green, Ohio 43403, United States*

Jiamin Huang − *Department of Physics, Bowling Green State University, Bowling Green, Ohio 43403, United States*

https://doi.org/10.1021/acsnano.4c02907
ACS Nano 2024, 18, 14661−14671

Jacob Beavon − *Department of Physics, Bowling Green State University, Bowling Green, Ohio 43403, United States*
Dulanjan Harankahage − *Department of Chemistry and The Center for Photochemical Sciences, Bowling Green State University, Bowling Green, Ohio 43403, United States*
Chao Yang Lin − *Robinson Research Institute, Victoria University of Wellington, Wellington 6012, New Zealand*
Kai Chen − *MacDiarmid Institute for Advanced Materials and Nanotechnology, Wellington 6012, New Zealand; Robinson Research Institute, Victoria University of Wellington, Wellington 6012, New Zealand; The Dodd-Walls Centre for Photonic and Quantum Technologies, University of Otago, Dunedin 9016, New Zealand*
Dries Van Thourhout − *Photonics Research Group, Ghent University, Gent 9000, Belgium;* orcid.org/0000-0003-0111-431X
Mikhail Zamkov − *The Center for Photochemical Sciences, Bowling Green State University, Bowling Green, Ohio 43403, United States; Department of Physics, Bowling Green State University, Bowling Green, Ohio 43403, United States;* orcid.org/0000-0002-8638-2972
Pieter Geiregat − *Physics and Chemistry of Nanostructures and NOLIMITS Core Facility for Non-Linear Microscopy and Spectroscopy, Ghent University, Gent 9000, Belgium;* orcid.org/0000-0001-7217-8738

Complete contact information is available at: https://pubs.acs.org/10.1021/acsnano.4c02907

Notes

The authors declare no competing financial interest.

ACKNOWLEDGMENTS

The work of the Zamkov group was supported by the NSF award #2208834. A.W. acknowledges the support by DE-SC0016872 funded by the U.S. Department of Energy, Office of Science. I.T. acknowledges funding from the IOF-STARTT Project "QD-LASER". C.Y. Lin and K.C. acknowledge support from the Marsden Fast-Start Fund by the Royal Society of New Zealand through contract VUW1715. P.G. acknowledges funding from the Research Foundation—Flanders (FWO-Vlaanderen under grant no. G037221N-HITEC), the SBO PROCEED project (no. S0002019N), and the Core Facility program NOLIMITS at Ghent University. D.V.T. acknowledges funding through FWO (G0B2921N).

REFERENCES

(1) Xie, W.; Stöferle, T.; Raino, G.; Aubert, T.; Bisschop, S.; Zhu, Y.; Mahrt, R. F.; Geiregat, P.; Brainis, E.; Hens, Z.; Van Thourhout, D. On-Chip Integrated Quantum-Dot−Silicon-Nitride Microdisk Lasers. *Adv. Mater.* **2017**, *29*, 1604866.
(2) Zhu, Y.; Xie, W.; Bisschop, S.; Aubert, T.; Brainis, E.; Geiregat, P.; Hens, Z.; Van Thourhout, D. On-Chip Single-Mode Distributed Feedback Colloidal Quantum Dot Laser under Nanosecond Pumping. *ACS Photonics* **2017**, *4*, 2446−2452.
(3) Tanghe, I.; Samoli, M.; Wagner, I.; Cayan, S. A.; Khan, A. H.; Chen, K.; Hodgkiss, J.; Moreels, I.; Van Thourhout, D.; Hens, Z.; et al. Optical gain and lasing from bulk cadmium sulfide nanocrystals through bandgap renormalization. *Nat. Nanotechnol.* **2023**, *18*, 1423−1429.
(4) Ahn, N.; Livache, C.; Pinchetti, V.; Jung, H.; Jin, H.; Hahm, D.; Park, Y.-S.; Klimov, V. I. Electrically Driven Amplified Spontaneous Emission from Colloidal Quantum Dots. *Nature* **2023**, *617*, 79−85.
(5) Geiregat, P.; Houtepen, A. J.; Sagar, L. K.; Infante, I.; Zapata, F.; Grigel, V.; Allan, G.; Delerue, C.; Van Thourhout, D.; Hens, Z. Continuous-wave Infrared Optical Gain and Amplified Spontaneous Emission at Ultralow Threshold by Colloidal HgTe Quantum Dots. *Nat. Mater.* **2018**, *17*, 35−42.
(6) Bisschop, S.; Geiregat, P.; Aubert, T.; Hens, Z. The Impact of Core/shell Sizes on the Optical Gain Characteristics of CdSe/CdS Quantum Dots. *ACS Nano* **2018**, *12*, 9011−9021.
(7) Tanghe, I.; Llusar, J.; Climente, J. I.; Barker, A.; Paternò, G.; Scotognella, F.; Polovitsyn, A.; Khan, A. H.; Hens, Z.; Van Thourhout, D.; et al. Role of Thermally Occupied Hole States in Room-Temperature Broadband Gain in CdSe/CdS Giant-Shell Nanocrystals. *Adv. Opt. Mater.* **2022**, *10*, 2201378.
(8) Geiregat, P.; Tomar, R.; Chen, K.; Singh, S.; Hodgkiss, J. M.; Hens, Z. Thermodynamic Equilibrium between Excitons and Excitonic Molecules Dictates Optical Gain in Colloidal CdSe Quantum Wells. *J. Phys. Chem. Lett.* **2019**, *10*, 3637−3644.
(9) Geuchies, J. J.; Dijkhuizen, R.; Koel, M.; Grimaldi, G.; du Fossé, I.; Evers, W. H.; Hens, Z.; Houtepen, A. J. Zero-threshold Optical Gain in Electrochemically Doped Nanoplatelets and the Physics Behind It. *ACS Nano* **2022**, *16*, 18777−18788.
(10) Li, X.; Du, J.; Zhao, G.; Zhang, B.; Livache, C.; Ahn, N.; Jia, Y.; Li, M.; Chen, Y.; Zhu, J.; Guo, J.; Klimov, V. I.; Wu, K. Two-Color Amplified Spontaneous Emission from Auger-Suppressed Quantum Dots in Liquids. *Adv. Mater.* **2024**, *36*, 2308979.
(11) Christodoulou, S.; Climente, J. I.; Planelles, J.; Brescia, R.; Prato, M.; Martín-García, B.; Khan, A. H.; Moreels, I. Chloride-Induced Thickness Control in CdSe Nanoplatelets. *Nano Lett.* **2018**, *18*, 6248−6254.
(12) Kelestemur, Y.; Guzelturk, B.; Erdem, O.; Olutas, M.; Gungor, K.; Demir, H. V. Platelet-in-Box Colloidal Quantum Wells: CdSe/CdS@CdS Core/Crown@Shell Heteronanoplatelets. *Adv. Funct. Mater.* **2016**, *26*, 3570−3579.
(13) Altintas, Y.; Gungor, K.; Gao, Y.; Sak, M.; Quliyeva, U.; Bappi, G.; Mutlugun, E.; Sargent, E. H.; Demir, H. V. Giant Alloyed Hot Injection Shells Enable Ultralow Optical Gain Threshold in Colloidal Quantum Wells. *ACS Nano* **2019**, *13*, 10662−10670.
(14) Leemans, J.; Singh, S.; Li, C.; Ten Brinck, S.; Bals, S.; Infante, I.; Moreels, I.; Hens, Z. Near-Edge Ligand Stripping and Robust Radiative Exciton Recombination in CdSe/CdS Core/Crown Nanoplatelets. *J. Phys. Chem. Lett.* **2020**, *11*, 3339−3344.
(15) Cassidy, J.; Diroll, B. T.; Mondal, N.; Berkinsky, D. B.; Zhao, K.; Harankahage, D.; Porotnikov, D.; Gately, R.; Khon, D.; Proppe, A.; Bawendi, M. G.; Schaller, R. D.; Malko, A. V.; Zamkov, M. Quantum Shells Boost the Optical Gain of Lasing Media. *ACS Nano* **2022**, *16*, 3017−3026.
(16) Harankahage, D.; Cassidy, J.; Beavon, J.; Huang, J.; Brown, N.; Berkinsky, D. B.; Marder, A.; Kayira, B.; Montemurri, M.; Anzenbacher, P.; et al. Quantum Shell in a Shell: Engineering Colloidal Nanocrystals for a High-Intensity Excitation Regime. *J. Am. Chem. Soc.* **2023**, *145*, 13326−13334.
(17) Das Sarma, S.; Jalabert, R.; Yang, S.-R. E. Band-gap Renormalization in Semiconductor Quantum Wells. *Phys. Rev. B* **1990**, *41*, 8288−8294.
(18) Tomar, R.; Kulkarni, A.; Chen, K.; Singh, S.; Van Thourhout, D.; Hodgkiss, J. M.; Siebbeles, L. D.; Hens, Z.; Geiregat, P. Charge Carrier Cooling Bottleneck Opens Up Nonexcitonic Gain Mechanisms in Colloidal CdSe Quantum Wells. *J. Phys. Chem. C* **2019**, *123*, 9640−9650.
(19) Kunneman, L. T.; Schins, J. M.; Pedetti, S.; Heuclin, H.; Grozema, F. C.; Houtepen, A. J.; Dubertret, B.; Siebbeles, L. D. Nature and Decay pathways of Photoexcited States in CdSe and CdSe/CdS nanoplatelets. *Nano Lett.* **2014**, *14*, 7039−7045.
(20) Cai, C.-S.; Lai, W.-Y.; Liu, P.-H.; Chou, T.-C.; Liu, R.-Y.; Lin, C.-M.; Gwo, S.; Hsu, W.-T. Ultralow Auger-Assisted Interlayer Exciton Annihilation in WS_2/WSe_2 Moiré Heterobilayers. *Nano Lett.* **2024**, *24*, 2773−2781.
(21) Akahane, Y.; Asano, T.; Song, B.-S.; Noda, S. High-Q photonic Nanocavity in a Two-dimensional Photonic Crystal. *Nature* **2003**, *425*, 944−947.

(22) Yoshida, M.; Katsuno, S.; Inoue, T.; Gelleta, J.; Izumi, K.; De Zoysa, M.; Ishizaki, K.; Noda, S. High-brightness Scalable Continuous-wave Single-mode Photonic-crystal Laser. *Nature* **2023**, *618*, 727−732.
(23) Adachi, M. M.; Fan, F.; Sellan, D. P.; Hoogland, S.; Voznyy, O.; Houtepen, A. J.; Parrish, K. D.; Kanjanaboos, P.; Malen, J. A.; Sargent, E. H. Microsecond-sustained Lasing from Colloidal Quantum Dot Solids. *Nat. Commun.* **2015**, *6*, 8694.
(24) Fan, F.; Voznyy, O.; Sabatini, R. P.; Bicanic, K. T.; Adachi, M. M.; McBride, J. R.; Reid, K. R.; Park, Y.-S.; Li, X.; Jain, A.; et al. Continuous-wave lasing in colloidal quantum dot solids enabled by facet-selective epitaxy. *Nature* **2017**, *544*, 75−79.
(25) Yokoyama, M.; Noda, S. Finite-difference Time-domain Simulation of Two-dimensional Photonic Crystal Surface-emitting Laser. *Opt. Express* **2005**, *13*, 2869−2880.
(26) Sakai, K.; Miyai, E.; Sakaguchi, T.; Ohnishi, D.; Okano, T.; Noda, S. Lasing Band-edge Identification for a Surface-emitting Photonic Crystal Laser. *IEEE J. Sel. Areas Commun.* **2005**, *23*, 1335−1340.
(27) Wang, Z.; Wang, P.; Lu, H.; Meng, B.; Wang, Y.; Tong, C.; Wang, L. Symmetry Criterion and Far-field Control of Photonic-crystal Surface-emitting Lasers. *Appl. Sci.* **2022**, *12*, 10581.
(28) Riechel, S.; Kallinger, C.; Lemmer, U.; Feldmann, J.; Gombert, A.; Wittwer, V.; Scherf, U. A Nearly Diffraction Limited Surface Emitting Conjugated Polymer Laser utilizing a Two-dimensional Photonic Band Structure. *Appl. Phys. Lett.* **2000**, *77*, 2310−2312.
(29) Ahn, N.; Park, Y.-S.; Livache, C.; Du, J.; Gungor, K.; Kim, J.; Klimov, V. I. Optically Excited Lasing in a Cavity-Based, High-Current-Density Quantum Dot Electroluminescent Device. *Adv. Mater.* **2023**, *35*, 2206613.
(30) Chen, K.; Gallaher, J. K.; Barker, A. J.; Hodgkiss, J. M. Transient Grating Photoluminescence Spectroscopy: An Ultrafast Method of Gating Broadband Spectra. *J. Phys. Chem. Lett.* **2014**, *5*, 1732−1737.

https://doi.org/10.1021/acsnano.4c02907
ACS Nano 2024, 18, 14661−14671